3D Analyze of the Cavitation Mechanism in Turbulent Flow using Partially-Average Navier Stokes Model around the Clark-y Hydrofoil

H. Kanfoudi[†], A. Bel Hadj Taher and R. Zgolli

Laboratory of Hydraulic and Environmental Modeling, National Engineering School of Tunis, University of Tunis EL MANAR, 1002 Tunis, Tunisia

†*Corresponding Author Email: hatem.kanfoudi@enit.utm.tn*

ABSTRACT

In order to accurately and reliably analyze in details the cavitation mechanism and their impact on flow structures, a three-dimensional unsteady cavitating turbulent flow around the three-dimension Clark-y hydrofoil is investigated be using a Partially-Average Navier Stokes (PANS) model based on Shear Stress Transport (SST). To track the interface of the liquid and the vapor, a Volume of Fluid (VOF) model is employed based on homogeneous mixture approach. To capture the interaction between the cavitation and the flow structure, a bridging method (PANS) between RANS and DNS have been chosen. This technique is able to resolve the unsteady turbulent structures by employing a more consistent methodology. The present numerical results are validated with experimental data. The interaction between the cavitation and the fluid vortex is analyzed and discussed. The numerical results show the capability of the presented model to predict the re-entrant jet and cavitation cloud shedding accurately.

Keywords: Clark-y hydrofoil; Cloud cavitation; Partially-average navier stokes; Vortex interaction; Unsteady flow; Fluid structure; OpenFoam.

NOMENCLATURE

C_D	drag coefficient	R	bubble radius
C_L	lift coefficient	R_0	initial radius of bubble
$Drag$	drag force	T_{ref}	reference time (time/shedding period)
Lift	lift force	U_∞	inlet flow velocity
$\dot{m}^+$	condensation source term	V_{vap}	volume of vapor in control cell
$\dot{m}^-$	vaporization source term		
n_0	nuclei concentration per unit volume of pure liquid	α_l	liquid volume fraction
		μ_l	vapor viscosity
n_0	nuclei concentration	μ_v	liquid viscosity
P_∞	outlet pressure	μ_t	eddy viscosity
P_v	vapor pressure	ρ_l	liquid density
		ρ_v	vapor viscosity

1. INTRODUCTION

The evolution of the mechanisms of the cloud cavitation produces a high-pressure fluctuation coming from the collapsing especially in the closure region at the trailing edge. This mechanism will cause material erosion which lead to a damage of the structure.

In hydraulic machinery, cavitation is encountered, it causes severe damage. The collapse of the bubble and the pocket of cavitation attached at the blade cause the erosion of the blade and it is the origin of the head drop. To understand this phenomenon, many authors have conducted research (Goncalves, Decaix, and Patella 2010; Wang and Su 2010; Salleo *et al.* 2000; Martynov 2005; .

In industrial, the cavitating flows are usually turbulent, and the interface between the vapor and liquid phases involves a complex interaction with the structure of the flow. These interactions are not well understood in the closure region of cavities.

Numerous aspects of cavitation have been studied by many investigators during the last several decades (Knapp, 1955)(Brennen, 1977)

A perturbed structure flow result in instabilities of the fluid flow causing periodic shedding of the cavitation pocket.

In order to enhance the study of perturbation of the structure flow in the developed the cavitating flow, various experimental measures have been performed. (Moussatov, Granger, and Dubus 2005; Suh and Lee 2008; Payri *et al.* 2012);

To measure the flow structure at the closure region (Moussatov, Granger, and Dubus 2005; Suh and Lee 2008; Payri *et al.* 2012; Yan and Thorpe 1990). (Katz, 1986), use a PIV. They concluded that the cavities in the closure region is highly unsteady. Furthermore, the collapse of the vapor cavity is responsible for the flow rotation.

Due to the limitation of the accessibility of the experimental techniques for the study of the mechanisms of detachment of the cavitation pocket. Several numerical methods evolved in parallel for study the unsteady cavitation shedding. The numerical simulations have been attracting many authors to predict the cavitating flow (Luo, X. w.; Ji, 2016)(Pendar, M. R.; Roohi, 2016)

Due to unsteady nature of the cavitating flow, it is imperative to model the cavitation flow with adequate turbulence models.

Referring to the literature, many turbulence model have been proposed like detached-eddy simulations (DES) (Travin *et al.*, 1999), the limited numerical scales method (LNS) (Batten, Goldberg and Chakravarthy, 2002), very large-eddy simulations (VLES) (Speziale, 1996) and Partially-Averaged Navier-Stokes (PANS) models (Girimaji, 2006).

(Sharath S. Girimaji, Ravi Srinivasan, 2003) compared the PANS model and LES, they concluded that, the PANS is suited for performing variable resolution simulation of the type sought with DES, hybrid RANS-LES, LNS and VLES.

(Girimaji and Abdol-hamid, 2006) realize a simulation in 2D flow past a cylinder using PANS model. They highlight that this methodology satisfies the requirements of a bridging model from RANS to DNS.

The PANS model has been also compared for a high and low Reynolds number with LES and DNS for simulating a flow past a circular cylinder. (Lakshmipathy and Togiti, 2011) proves that the PANS model can provide good results on the wide range of Reynolds number.

(Luo *et al.*, 2014) realize a comparative assessment of PANS and DES simulation in 3D of flow past cylinder. They prove that the PANS model is able to simulate the separate flow.

(Ranjan and Dewan, 2015) found that the PANS model predicts the mean quantities of all flow features for simulation a flow past a rectangular cylinder.

In this paper, we are interested to investigate numerically in 3D the unsteady cavitating flow based on the transport equation model (TEM) with source term (Kanfoudi, 2015). For turbulence modeling, we used the SST-PANS model. The main objective of this paper is to study the ability of the SST-PANS for capturing the flow structure in 3D and analyzing the impact of the cavity growth and shedding on the flow fluid over a Clark-y hydrofoil. The numerical simulation is carried out with OpenFOAM and the validation of the numerical solution is based on the experimental results of (Huang *et al.*, 2013)

2. MATHEMATICAL FORMULATION

In this section, we present the Partially-Average Navier Stokes model (PANS) used to analyze the cavitating flow. The PANS model can be classified as a bridging method between the Reynolds Average Navier Stokes (RANS) and the Direct Numerical Simulation (DNS).

The governing equation for incompressible solver can be express as:

$$\frac{\partial U_i}{\partial x_i} = 0 \tag{1}$$

$$\frac{\partial U_i}{\partial t} + U_j \frac{\partial U_i}{\partial x_j} = -\frac{\partial P}{\partial x_j} + \nu_m \frac{\partial^2 U_i}{\partial x_j \partial x_j} - \frac{\partial \tau(V_i V_j)}{\partial x_j} \tag{2}$$

Where V_i is the instantaneous velocity field, it can be decomposed to a filtered field and the fluctuating part, $V_i = U_i + u_i$. To modeling the Sub Filtred Stres (SFS) $\tau(V_i V_j)$, a Boussinesq assumption is used :

$$\frac{\partial \tau(V_i V_j)}{\partial x_j} = -\nu_u \left(\frac{\partial U_i}{\partial x_j} + \frac{\partial U_j}{\partial x_i} \right) + \frac{2}{3} k_u \delta_{ij} \tag{3}$$

Where ν_u is the eddy viscosity. In this study, we use a $k-\omega$ Shear Stress Transport to calculated this eddy viscosity.

$$\rho_m \nu_u = \mu_u = \min \left(\frac{\rho k_u}{\omega_u}, \frac{a_1 \rho k_u}{SF_2} \right) \tag{4}$$

The k_u denotes the unresolved turbulent kinetic energy and ω_u the unresolved dissipation rate.

2.1 Partially-Average Navier Stokes Model

The idea behind the PANS is to separate the energy of the large flow structure which is

generated from the mean flow and then transfer it to smaller flow structure in the energy cascade. The smaller flow structure is modeled by the eddy viscosity v_u. This latter is calculated by two transport equation:

Unresolved Turbulent kinetic energy equation

$$\frac{\partial(\rho k_u)}{\partial t} + \frac{\partial(\rho U_i k_u)}{\partial x_i} = P_{k_u} - \beta^* \rho k_u \omega_u$$
$$+ \frac{\partial}{\partial x_i}\left[\left(\mu + \sigma_{k_u}\mu_u\right)\frac{\partial k_u}{\partial x_i}\right] \tag{5}$$

Unresolved Turbulent frequency equation:

$$\frac{\partial(\rho \omega_u)}{\partial t} + \frac{\partial(\rho U_i \omega_u)}{\partial x_i} = \frac{\gamma}{v_u} P_{k_u} - \beta' \rho k_u \omega_u^2$$
$$+ \frac{\partial}{\partial x_i}\left[\left(\mu + \sigma_{\omega_u}\mu_u\right)\frac{\partial \omega_u}{\partial x_i}\right] + 2\left(1 + F_1\right)\frac{\rho \sigma_{\omega 2u}}{\sigma_{\omega_u}}\frac{\partial k_u}{\partial x_i}\frac{\partial \omega_u}{\partial x_i} \tag{6}$$

The modification from the original model are defined by :

$$\beta' = \gamma \beta^* - \frac{\gamma \beta}{f_\omega} + \frac{\beta}{f_\omega}; \quad \sigma_{k_u} = \sigma_k \frac{f_\omega}{f_k}; \quad \sigma_{\omega_u} = \sigma_\omega \frac{f_\omega}{f_k} \quad (7)$$

The value of the coefficients β^*, σ_k, and σ_ω are the same as the original model SST. The ratios of PANS model are:

$$f_k = \frac{k_u}{k}; \quad f_\omega = \frac{\omega_u}{\omega} = \frac{f_\varepsilon}{f_k} \tag{8}$$

Where the total turbulent kinetic energy is donated k and the total specific dissipation rate ω. The expressions for the two blending functions in the case of SST PANS are given by :

$$F_1 = \tanh\left\{\left\{\min\left[\max\left(\frac{\sqrt{k_u}}{\beta^* \omega_u d}, \frac{500\mu}{d^2 \rho \omega_u}\right)\right]^4, \frac{4\rho \sigma_{\omega 2u} k_u}{CD_{k\omega} d^2}\right\}\right\} \tag{9}$$

$$CD_{k\omega} = \max\left(\frac{2\rho \sigma_{\omega 2u}}{\omega_u}\frac{\partial k_u}{\partial x_i}\frac{\partial \omega_u}{\partial x_i}, 10^{-10}\right) \tag{10}$$

$$F_2 = \tanh\left\{\left[\max\left(\frac{2\sqrt{k_u}}{\beta^* \omega_u d}, \frac{500\mu}{d^2 \rho \omega_u}\right)\right]\right\} \tag{11}$$

For a value of $f_k = 1$ and $f_\omega = 1$, the PANS model will be reduced to RANS model. To switch to the DNS, a lowing value of f_k and f_ω are required for bridging to Navier–Stokes when the grid is not fine (Girimaji and Abdol-hamid, 2006, Girimaji, 2016).

Physically, in cavitating flow, the large scale contains the kinetic energy responsible for the development of the cavitation pocket. The dissipation of the energy inducing the small scale favoring the formation of the re-entrant jet leading

to the cloud cavity shedding.

In this study, a value of f_ω is set to unity and for the f_k a dynamic value is update spatially according to this expression:

$$f_k = \min\left[C_{PANS}\left(\frac{\Delta}{l_u}\right)^{2/3}, 1\right]$$
$$l_u = \frac{\sqrt{k_u}}{\beta^* \omega_u} \tag{12}$$

Where $\Delta = \sqrt[3]{\left(\Delta x \times \Delta y \times \Delta z\right)}$ represent the grid scale and l_u the unresolved turbulent length scale. The value of C_{PANS} is set to 0.1 Luo *et al.* 2014.

2.2 Physical Cavitation Model

The cavitation model is based on the homogenous flows mixture, a spatial distribution of the two phase (liquid and vapour) is specified by applying a volume fraction of liquid α_l. Hence, the mixture density ρ_m and mixture viscosity v_m can be defined as a function of α_l :

$$\rho_m = \rho_l \alpha_l + \left(1 - \alpha_l\right)\rho_v$$
$$v_m = v_l \alpha_l + \left(1 - \alpha_l\right)v_v \tag{13}$$

To calculate the volume fraction of liquid, a solving transport equation of α_l is employed:

$$\frac{\partial(\rho_l \alpha_l)}{\partial t} + \frac{\partial(\alpha_l \rho_l U_i)}{\partial x_i} = \dot{m}^+ - \dot{m}^- \tag{14}$$

where m^+ and m^- are the mass transfer rate for the production and the destruction of the liquid. In this study, the (Kanfoudi, 2011, Kanfoudi, 2015, Kanfoudi and Zgolli, 2014) model is employed. The mass transfer of the TEM are :

$$\dot{m}^- = C_e\left(1 - \alpha_l\right)^{\frac{2}{3}}\alpha_l^{\frac{4}{3}}\frac{\rho_v \rho_l}{\rho_m}\sqrt{\frac{2}{3}\frac{p_v - p}{\rho_l}} \tag{1}$$

$$\dot{m}^+ = C_c\left(1 - \alpha_l\right)^{\frac{1}{6}}\alpha_l^2\frac{\rho_v \rho_l}{\rho_m}\sqrt{\frac{2}{3}\frac{p - p_v}{\rho_l}} \tag{16}$$

With

$$C_c = -10 R_0^{\frac{3}{2}} n_0^{\frac{5}{6}}$$
$$C_e = 5\sqrt[3]{n_0} \tag{17}$$

This two parameter are related by the expression of the vapor volume fraction (Yuan *et al.* 2001).

The value of nuclei concentration $n_0 = 10^{13}$ nuclei/m$^3_{water}$ and the initial bubble radius $R_0 = 1\,\mu m$ (Kanfoudi, 2011).
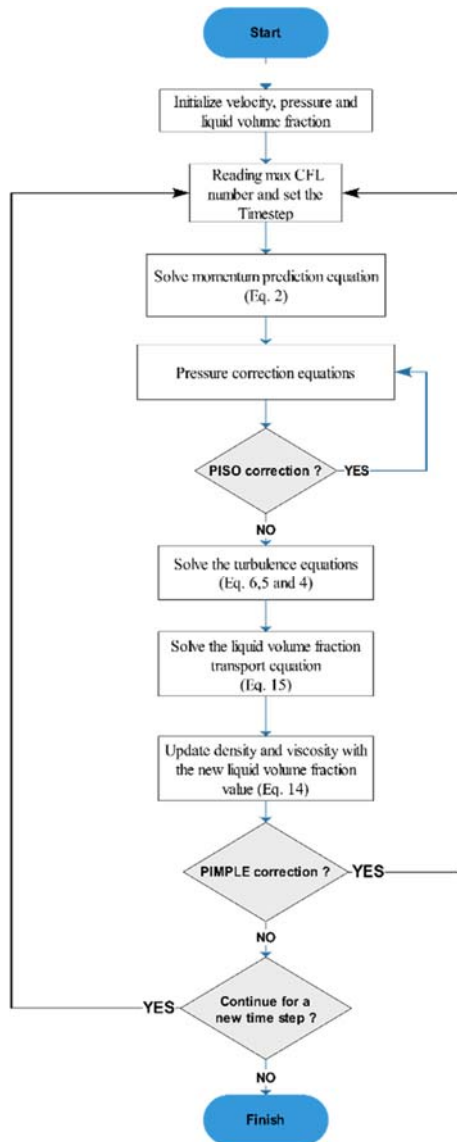
Fig. 1. Solver algorithm.

3. NUMERICAL METHODOLOGY

3.1 Solution Procedure

The model equations presented in previous section were solved within the open source CFD code OpenFoam 4.1.

The equations of the mass, momentum, turbulence and scalar transport equations were solved in a segregated is calculated based on interface capturing.

For the mass transfer terms of the transport equation of the volume fraction of liquid a (Kanfoudi, 2015) model is implemented and compiled.

Due to the dependence of the volume fraction of liquid on the pressure and also the velocity, we choose a pressure implicit spilling of operators (PISO) procedure for velocity-pressure correction. As the numerical solution is unsteady, a pimple solver is employed for simulation an unsteady

cavitation in turbulent flow.

The numerical solution is controlled by set of a residual of the pressure, velocity and the turbulence model in each iteration equal to 10^{-7} and 10^{-9} for the transport equation of the volume fraction of liquid.

The time step is adjusted according to the CFL number which is set the maximum to 1. The value of the time step is modified according to this value. The Fig. 1 show the solver algorithm employed in this study for simulation the cavitation on a turbulent flow.

3.2 Simulation Setup

In this section, we present the numerical setup used to analyze the unsteady cavitating flow. A 3D configuration domain is adopted for captured the mechanism of the formation, entrainment and the collapse of a cloud cavitation shedding. The hydrofoil geometry employed is a Clark-y with a chord c=70mm and 70 mm span length. To reduce the computation resource a half of the spanwise is adopted with symmetry condition. The hydrofoil has an angle of attack of 8° (see Fig. 2).
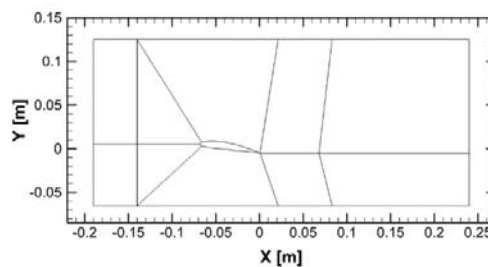

Fig. 2. Computation domain.

For the mesh generation, we use a grid with H-topology around the hydrofoil, which is practice to capture the viscous forces.
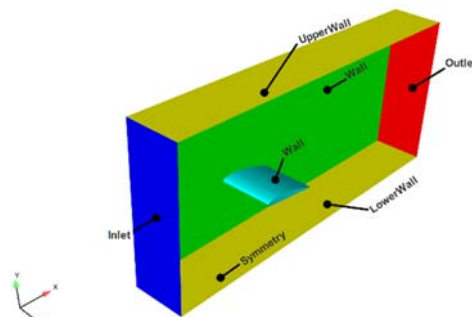

Fig. 3. 3D configuration of the computation domain.

In Fig. 3 we present the 3D computation domain with the boundary condition used in the numerical simulation. Totally, we specified six boundary conditions, the Table 1 describe the type of condition of each boundary. In Fig. 3 we present the 3D computation domain with the boundary condition used in the numerical simulation. Totally, we specified six boundary conditions, the Table 1 describe the type of condition of each boundary.

Table 1 Numerical values of boundary conditions

Boundary	Velocity	Pressure	ω_u	k_u	ν_u	α_t
Inlet	fixedValue	zeroGradient	fixedValue	fixedValue	Calculated	fixedValue
Outlet	zeroGradient	fixedValue	zeroGradient	zeroGradient	zeroGradient	zeroGradient
Wall	no slip	zeroGradient	omegaWall Function	kqRWall Function	nutkWallFunction	zeroGradient
UpperWall	Slip	zeroGradient	zeroGradient	zeroGradient	zeroGradient	zeroGradient
LowerWall	Slip	zeroGradient	zeroGradient	zeroGradient	zeroGradient	zeroGradient
Symmetry	Symmetry Plane	Symmetry Plane	symmetryPlane	Symmetry Plane	symmetryPlane	symmetryPlane

Table 2 Mesh independence test

Mesh resolution		$\Delta x = \Delta y = \Delta z$	C_l	C_d	C_l Error (%)	C_D Error (%)
Mesh 1	coarse	0.002	0.832	0.1184	9.47	-0.50
Mesh 2	medium	0.001	0.755	0.1188	-0.66	-0.17
Mesh 3	fine	0.0005	0.757	0.1189	-0.39	-0.08
Experimental			0.760	0.1190	-	-

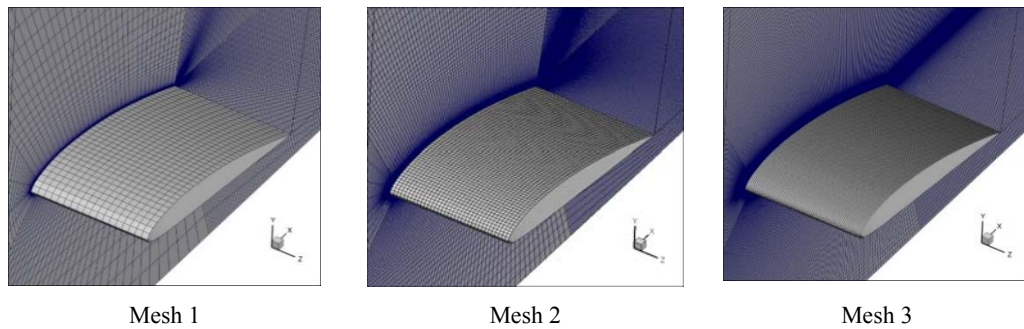| Mesh 1 | Mesh 2 | Mesh 3 |

Fig. 4. Three tested structured grid.

At the inlet a fixed value of the velocity is used $U = 10$ m/s, which correspond to Reynolds number 710^7, at the outlet a constant pressure was specified as a function of $\sigma = 0.8$.

Due to the influence of the mesh into the simulation results, a structured gird with ten blocks (see Fig. 2) is applied, this choice leads to capture the boundary layer, the pressure gradient and the flow separation at the trailing edge of the hydrofoil.

To modeling accurate, the boundary layer on the wall, we used a wall function for turbulence kinetic energy k_u a kqWallFunction with a uniform value with is recommended for a high Reynolds number, for the rate of dissipation ω_u choose the omegaWallFunction wall function with a fixed value. To capture numerically the boundary layer a value of $x^+ = y^+ = 1$ is used. For the eddy viscosity ν_u at the wall we employed a nutkWallFunction which provides a turbulence viscosity condition based on the turbulence kinetic energy.

To verify the dependence of the numerical solution from the mesh, we tested three meshes in transient regime. The criteria of the selected are based on the average value of the lift and drag coefficients compared to the experimental measure. The expressions of these coefficients are expressed as follows:

$$C_L = \frac{Lift}{\frac{1}{2}\rho_l U^2 A} \quad C_D = \frac{Drag}{\frac{1}{2}\rho_l U^2 A} \tag{18}$$

In Fig. 4, we present three meshes tested. The details of the mesh spacing and the numerical results of hydrodynamics coefficient are compared to the experimental measure are reported in Table 2.

Referring to comparison of the drag and the lift coefficients of the three mesh used (see Table2) with experimental, we remark for the drag coefficient, the mesh quality does not have, this is due to the value of $x^+ = y^+ = 1$ applied to modeling the boundary layer, which is independent of the number of the node.

Concerning the lift coefficient, we remark as the number of the node increases the numerical results approach the experimental. Comparing the medium
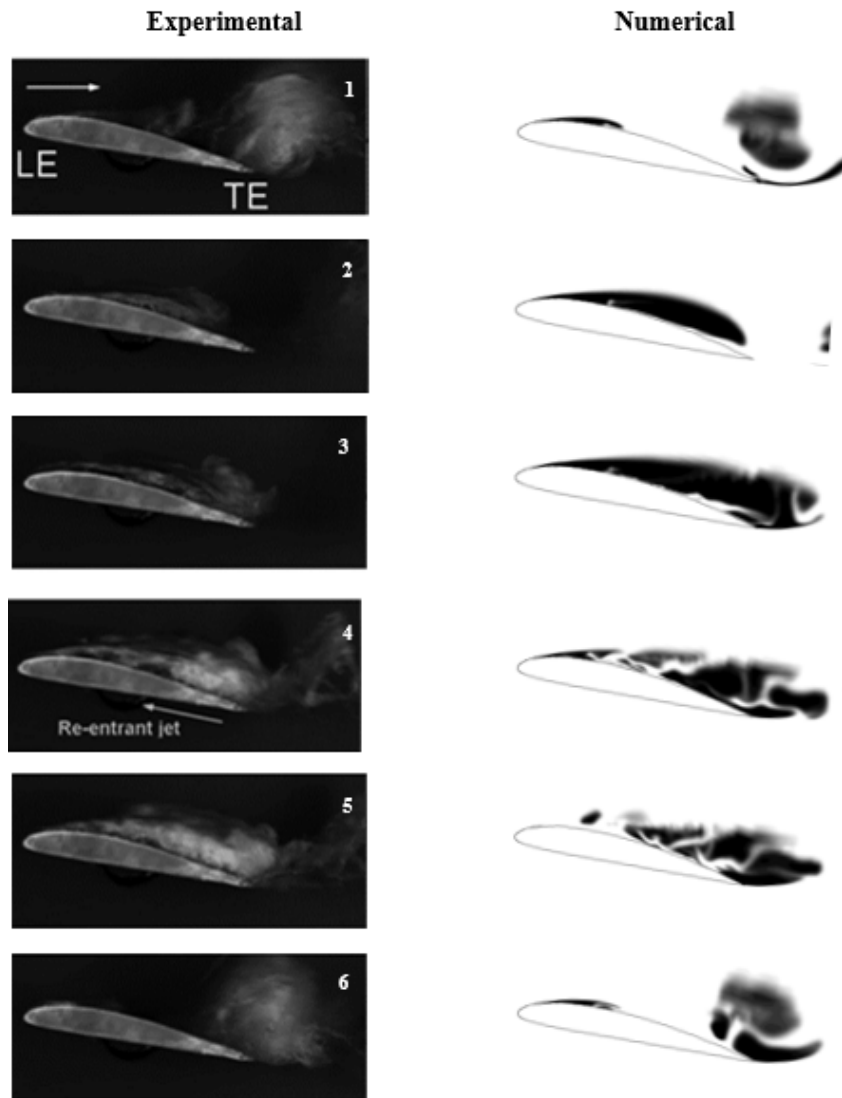
Experimental   Numerical

Fig. 5. Comparison of the experimental visualization (Huang *et al.*, 2013). and numerical simulation of the cavitation shedding.

and the fine grid, we found that there is not a significate difference concerning the value of the lift coefficient and the cavity detachment.

Overall, we can choose the medium mesh for simulation unsteady the cavitating flow coupling with PANS model.

For the computing resources, the unsteady computations are done using Dell PowerEdge 720 with 16 processors (4 sockets and 4 cores) Intel® Xeon® E5-2600 2.2 GHz and 64 Go Ram memory.The CPU time for each cycle of cavitation shedding is about 6 hours.

4. RESULTS AND DISCUSSION

The numerical simulation in this paper, aim to analyze and study the dynamics mechanism of the sheet cavitation shedding using a PANS model. The validation of this numerical model is performed with the experimental measurement available from (Huang *et al.*, 2013).

To evaluate the numerical model with the experimental visualization, a six snapshots are presented in Fig. 5. In this figure, a time evolution of cavitation shedding for a one typical cycle are compared.

As shown in Fig. 5.1, numerically and experimentally the sheet cavity starts to grow at the leading edge, we can observe the vapor pocket is convected at the trailing edge from the preview cavity shedding.

At Figs. 5.2 and 5.3, the attached cavity growth continuously and seems to be stable. At mi-chord we observe that the cavity separates from the extrados of the hydrofoil. At Fig. 5.4, we highlight both numerically and experimentally a reverse flow at the trailing edge inducing a re-entrant jet.

In Fig. 5.5, the sheet vapor is split to a small sheet vapor, this mechanism is due to the re-entrant jet, which is generated at the trailing edge of the hydrofoil and continuous to move to the leading edge.
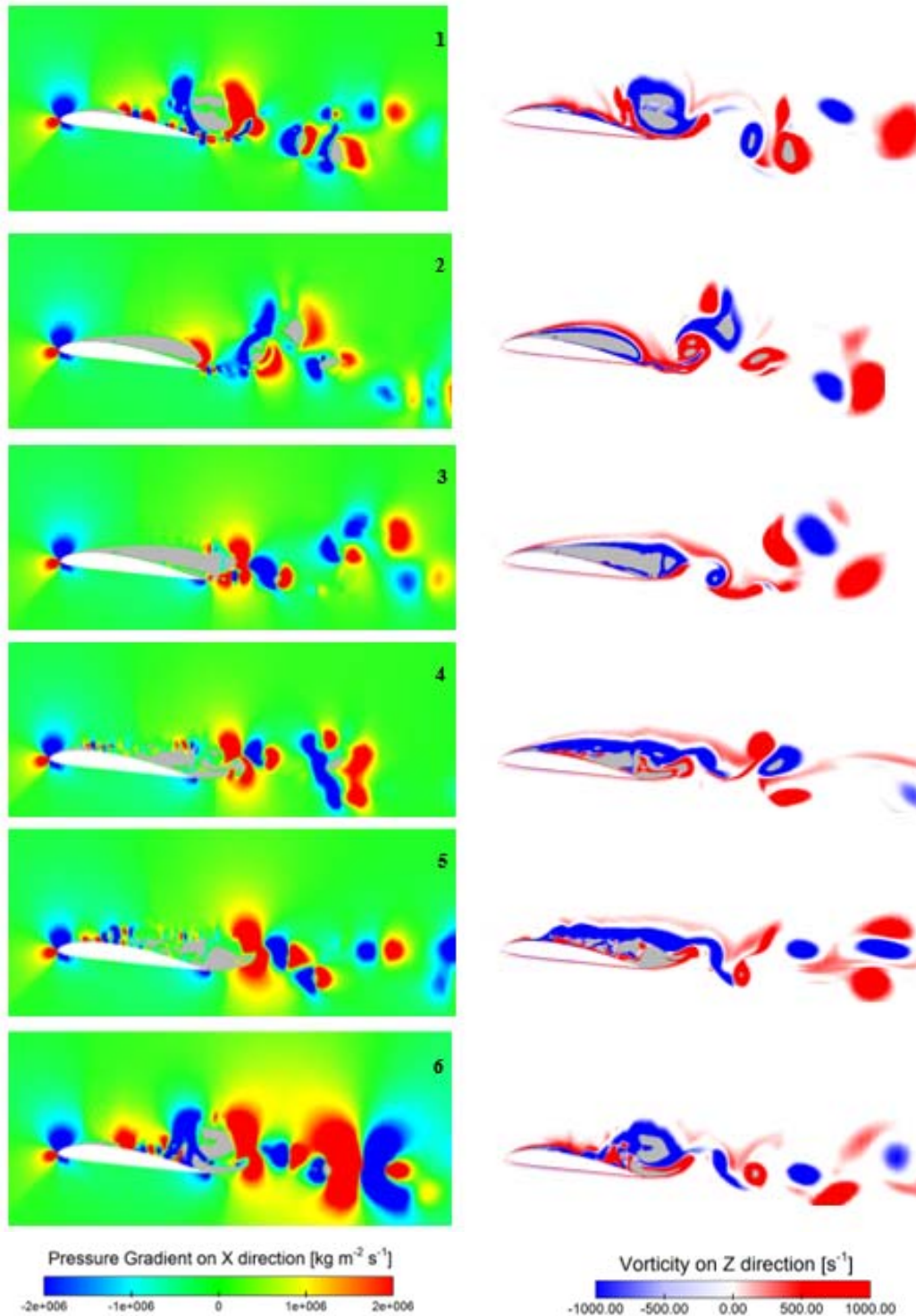
Fig. 6. Pressure gradient (at the left) and the vorticity production (at the right).

After the split of the main sheet vapor (Fig. 5.6), the small sheet is convected far away from the hydrofoil, and the leading edge is free.

It is evident that the numerical model can predict the production and the evolution of the sheet of the vapor comparing to the experimental.

To better analyses the mechanism of the cavitation shedding, we present in Fig. 6 the pressure gradient distribution on the x-direction and the vorticity induced by the detachment of the vapor cavity at the middle of the span of the hydrofoil.

At time 1, at the leading edge of the hydrofoil, a negative pressure gradient is responsible of the growth and the convection of the sheet cavity. From the previous cycle, the shed cavity is around by a negative pressure gradient in front and positive pressure gradient at the back, this pressure gradient

will cause the rotation of the shed cavity. In this time, the shed cavity it is responsible of the flow perturbation and generation of the turbulence causing a production of vorticity at the trailing edge of the hydrofoil.

At time 2, the sheet cavity continuous to growth due to flow convection and reached the maximum length. As the sheet cavity became thicker, it will be comported like an obstacle in flow field.

A time 3, the main sheet cavity will cause a flow separation in the closure region, favoring a change of the pressure gradient to a positive pressure at the rear of the pocket. This gradient will generate a re-entrant jet.

At time 4 and 5, the re-entrant start to travels upstream along the extrados of the hydrofoil. The reversed flow will lead to rupture of the interface between the vapor pocket and the wall. And as a result the split and the fragmentation of the main cavity vapor.

After the split and convection of the sheet cavity, we notice a high pressure gradient at the trailing edge, this fluctuation of the pressure in this region will induced a vibration and erosion of the hydrofoil material. Now the leading edge is free of the cavity vapor, a new cycle of the vapor sheet starts to grow (time 6).

To capture the detachment of the shedding cavity numerically, we adopted the expression of the volume of the vapor V_{vap} on the calculated domain, the expression is given as follows:

$$V_{vap} = \sum_{i=1}^{N}(1-\alpha_i)V_i \qquad (19)$$

where N denote the number of the control volumes, α_i the vapor volume fraction occupied and the total volume of each control volume in the computational domain.

For practical reasons, all results are presented as dimensionless numbers in the following discussion.

To validate the numerical model, a comparison of the numerical model of the cavity volume with the experimental is presented in Fig. 7.

Based in the comparison (Fig. 7), we can confirm that the numerical model can reproduce the time evolution of the cavity vapor.

In Fig. 8, we present a validation of the numerical lift coefficient with the experimental. The numerical model is able to reproduce hydrodynamic pressure applied to the hydrofoil.

The ability of PANS model and the cavitation model to reproduce the cavitating behavior is justified by the comparison with the experimental data available.

In Fig. 9, both experimental and numerical time average u-velocity component are compared for four positions at x/c = 20 %, 40 %, 60 % and 80 %.

At the position 20 % and 40 %, we show the flow velocity is not perturbed, in this position the pocket cavity is stable which justifies this profile. For 60 % and 80 %, we observe a reverse flow, this is due to re-entrant flow induced by positive pressure gradient. Further in this region, a high rotational flow structure is generated.

It is clear that the numerical simulation is in good agreement with the experimental.
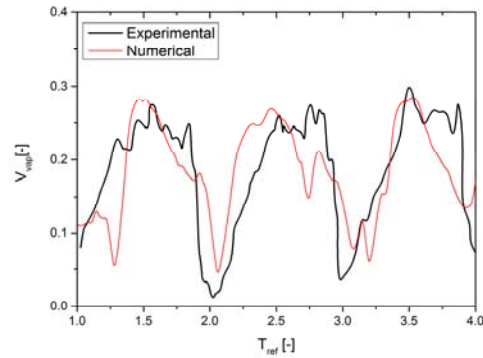

Fig. 7. Comparison between numerical and experimental of the cavity volume variation.
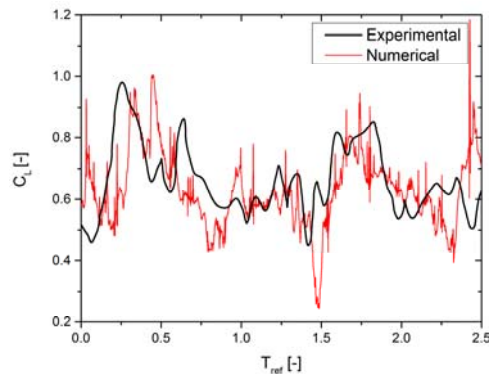

Fig. 8. Comparison between numerical and experimental fluctuating lift coefficient.

In order to understand the mechanisms of generation of the vapor cavity and its impact on the flow, we present in Fig. 10 the consequences of the evolution of a cavitation pocket on the lift and drag coefficients for five cycles.

As the volume of pocket increases, we remark that the drag coefficient decrease, this phenomenon can be explaining by the fact that the evolution of the cavity pocket at the extrados of the hydrofoil will destroy the boundary layer by the re-entrant jet, hence the drag force will be reduced at the minimum. The same for the lift coefficient, as the pocket cavity grow and reached its maximum, the hydrodynamic pressure applied to the extrados of the hydrofoil decrease and favoring the increase of the lift force.

In Fig. 11, wee plot the power spectrum density (PSD) of the vapor volume. By comparing PSD between the experimental and numerical, we can conclude that the numerical model is in concordance.
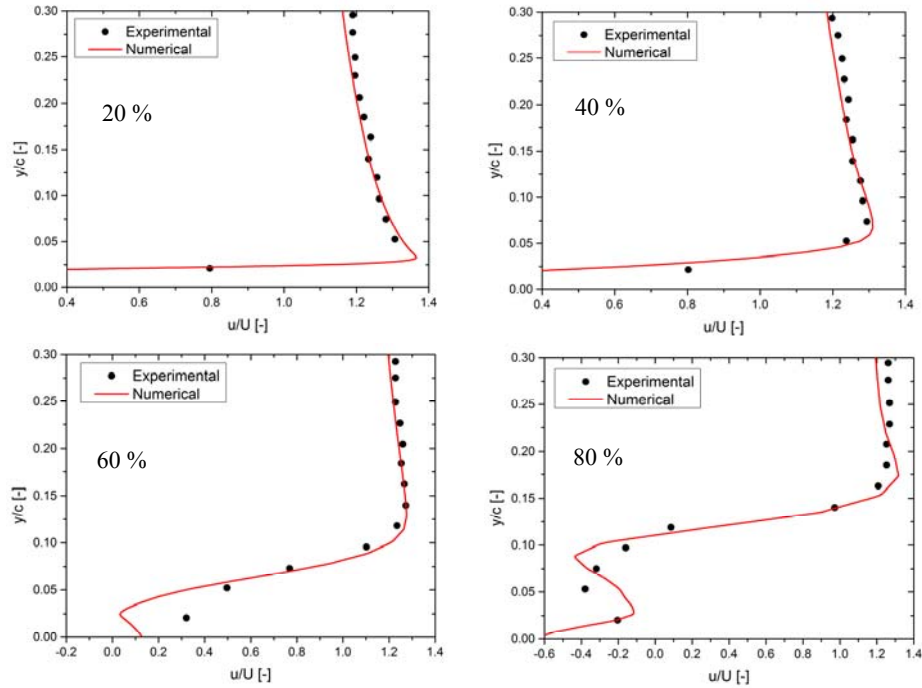
Fig. 9. Comparisons of the experimental and calculated average u velocity component.

From this figure, we can observe that the frequency of the detachment of the cavitation is $f = 22$ Hz. This frequency corresponds to the cycle evolution of the cavity with being corresponding to the large flow structure.
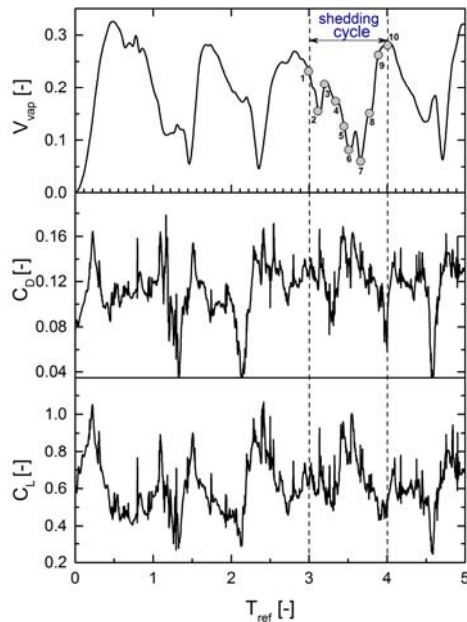

Fig. 10. Time evolution of the cavity pocket and coefficient of the lift and drag.

To study the interaction of the flow structure with the entrainment of the vapor cavity, we choose a cyclic behavior of the vapor sheet presented at ten equidistant time-instants (see Fig. 10). In Fig. 12, we present both the cavity vapor and the flow

structure. To visualize the vortex shells produced by the cavitation shedding a Q-criterion variable is used. The positive value of this latter

isolates the region where the rotation of flow overcome the strain. This variable is defined as :

$$Q = \frac{1}{2}\left(\Omega_{ij}\Omega_{ij} - S_{ij}S_{ij}\right) \qquad (20)$$

where $\Omega_{ij} = \left(u_{ij} - u_{ji}\right)/2$ and $S_{ij} = \left(u_{ij} + u_{ji}\right)/2$.
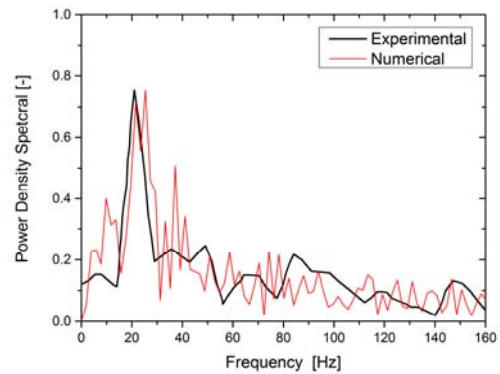

Fig. 11. Comparisons between experimental and numerical of the power spectrum density.

To better detect the vorticity generated by the cavitation shedding, the isosurface of the Q-criterion eliminates the production of the vorticity generated from the boundary layer and so visualize the flow structure issues from the cavity detachment.

In Fig. 12, we present the evolution of cavity shedding cycle and her impact on the structure of the flow, colored according to the flow velocity.
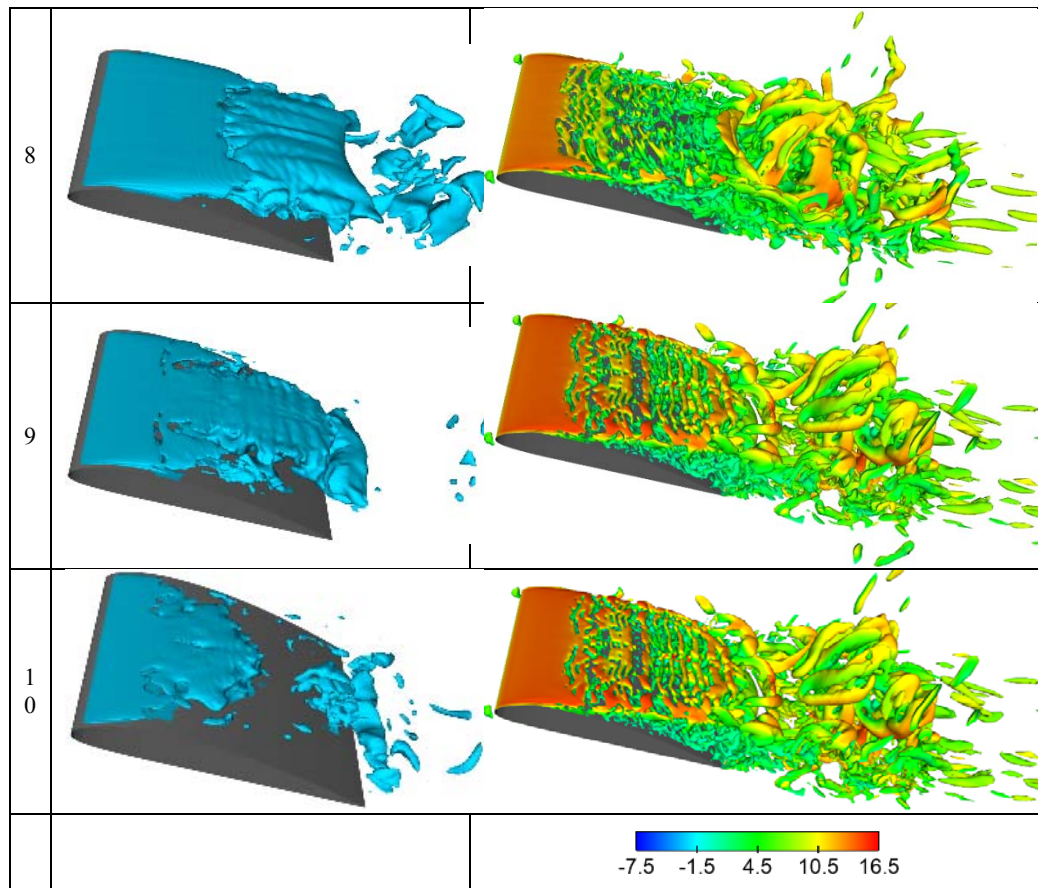
-7.5   -1.5   4.5   10.5   16.5
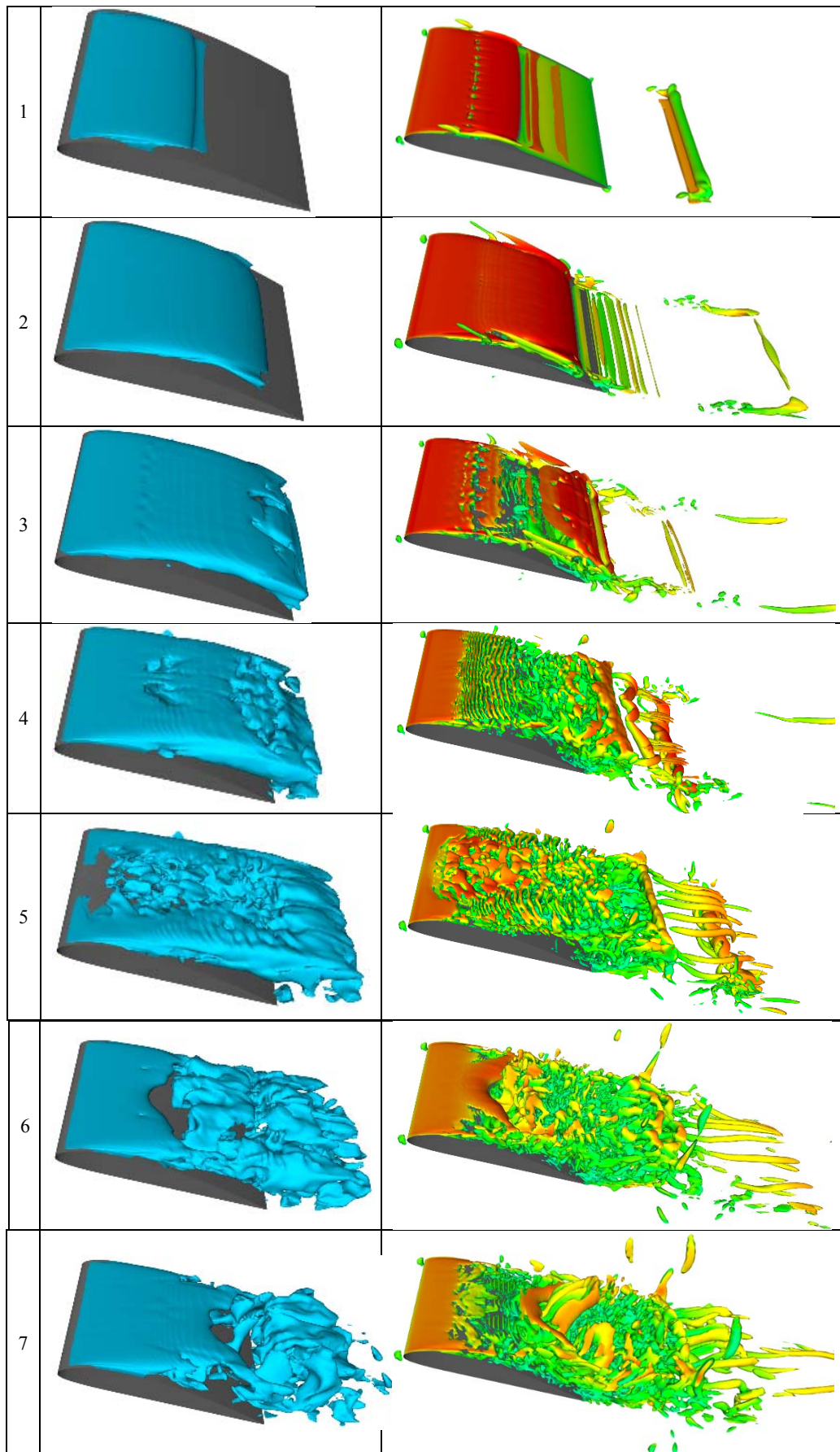
Fig. 12. Time Evolution of the cavity vapor at the left, and the flow structure at the right (colored by velocity).

From these numerical results, we can confirm that the vortex stretching occurs in the center of the cloud cavity. The core of the vortex also is generated at the region of the detachment of the cavity and evolved quasi-periodically at the same frequency of the large structure.

Referring to Figs. 12.1 and 12.2, the cavity continues to growth due to the negative pressure gradient, as well the cavity become thin, it will be like an obstacle, causing an acceleration of the flow velocity. This energy produced will be the source for generation the large eddies.

At the Figs. 12.3 to12-7, this energy is transfer to the mi-chord of the hydrofoil. In this region, the vapor cavity reaches the maximum length, the flow will re-attachment to the hydrofoil. Finally, at Figs. 12.8 to 12.10, a destruction of the large structure into small structure, this mechanism is recognized as the energy cascade.

The vortex stretching is mainly located at the trailing edge of the hydrofoil in the region of the reversed flow. At this position, the re-entrant jet induces the dramatic shedding of the cavitation cloud, and we can assume that these mechanisms are responsible of the production of the vorticity and the flow perturbation It is clear of the numerical results, that the cavitation is responsible for the production of the vortex stretching term.

In Fig. 13, a visualization of the attachment at separation flow over the hydrofoil, we highlight that the vapor cavity produces a perturbation and a high turbulence which is the origin of separation of the flow.
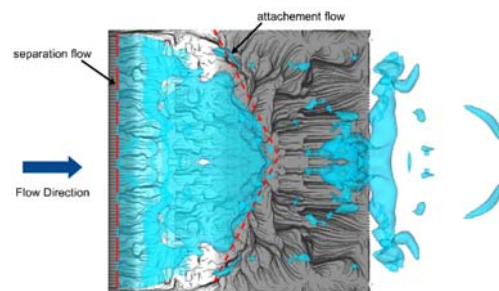

Fig. 13. Attachment and separation flow in the extrados of the hydrofoil at last time.

In Fig. 14, we present the energy spectrum of the energy cascade. The behavior of this energy exhibits a powerlaw with a slope equal to -5/3. This value was determined by Kolmogorov theory for a homogenous fluid Davidson and Peng, 2003. This result proves that the PANS turbulence model is able to capture the energy spectrum at high Reynolds number.

Overall, the present model clearly reproduces the

cavitation patterns and there evolution around the Clark-y hydrofoil and captures the behaviors of the re-entrant flow well and shows a good agreement with experimental observation.
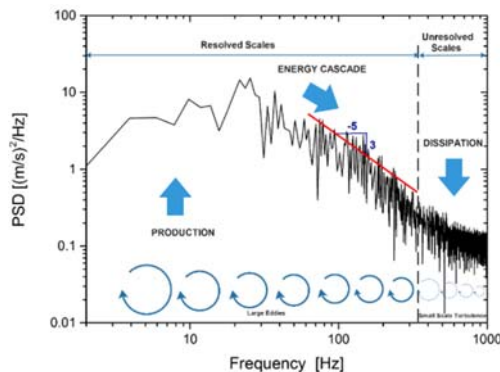

Fig. 14. Energy spectrum of the cavitating flow.

5. CONCLUSION

The 3D unsteady cavitating flow around a Clark-y hydrofoil was investigated numerically with OpenFoam using the SST-PANS model coupled with the Kanfoudi cavitation model.

The mechanisms dictating the flow behaviors and thecavitation shedding dynamics evolution with the cavitation-vortex interaction were examined and summarized.

The numerical results indicate that the cloud cavitation is responsible for the production of the vortex stretching term. The experimentally observed cavitating flow features are well reproduced by the numerical model results and the main conclusions are:

1. The Partially-Average Navier Stokes model, can capture and resolved the flows structures which is responsible of the production of the pressure positive gradient which induces the re-entrant jet. The predicted cavitation evolution agrees well with the experimental results.

2. To modeling the dynamic behavior of the detached cavity, we should choose a turbulence model able to capture the instability in the unsteady flow. As results, the PANS model predicted and modeled perfectly mechanisms of extraction of the cavitation pocket with reasonable costs and good accuracies

3. The present numerical model accurately predicts the formation of cavitation, with characteristic behavior and reproduces faithfully the mechanisms of re-entrant jet;

4. The SST-PANS turbulence model which is based on RANS formulation prove the encouraging capability of predicting the transient cavitating turbulent flows;

Finally, to summarize, the numerical results show that the coupling between the SST-PANS model with TEM model improve the accuracy of prediction the cavity shedding.

REFERENCES

Batten, P., U. Goldberg and S.Chakravarthy (2002) LNS-An approach towards embedded LES , *AIAA paper*, 2002−0427, 1−10.

Brennen, C. (1977) *Cavitation and bubble dynamics*, *Annual Review of Fluid Mechanics*.

Davidson, L. and S. H. Peng (2003) Hybrid LES-RANS modelling: A one-equation SGS model combined with a k-e model for predicting recirculating flows , *International Journal for Numerical Methods in Fluids* 43(9), 1003–1018.

Girimaji, S. S. (2006) Partially-Averaged Navier-Stokes Model for Turbulence: A Reynolds-Averaged Navier-Stokes to Direct Numerical Simulation Bridging Method , *Journal of Applied Mechanics* 73(3), 413.

Girimaji, S. S. (2016) Model for Turbulence: A Navier-Stokes to Direct Numerical, 73.

Girimaji, S. S. and K. S. Abdol-hamid (2006) Partially-averaged Navier Stokes Model for Turbulence : Implementation and Validation , *Journal of Applied Mechanics* 73(January), 413–421.

Goncalves, E., J. Decaix, and R. F. Patella (2010) Unsteady simulation of cavitating flows in Venturi , in *Journal of Hydrodynamics* 711–716.

Huang, B., Y. L. Young, G. Wang, and W. Shyy (2013) Combined Experimental and Computational Investigation of Unsteady Structure of Sheet/Cloud Cavitation , *Journal of Fluids Engineering* 135(7), 71301.

Kanfoudi, H. (2011) A numerical model to simulate the cavitating flows , *International Journal of Modeling, Simulation, and Scientific Computing* 2(3), 277–297.

Kanfoudi, H. (2015) Modeling and computation of the cavitating flow in injection nozzle holes , *International Journal of Modeling, Simulation, and Scientific Computing* 06(01), p. 1550003.

Kanfoudi, H. and R. Zgolli (2014) Simulation of unsteady cavitating flow aound an hydrofoil , in *IREC 2014   5th International Renewable Energy Congress*.

Katz, J. (1986) Cavitation in Large Scale Shear Flows , *Journal of Fluids Engineering* 108(September 1986), 373–376.

Knapp, R. T. (1955) Recent Investigations of the Mechanics of Cavitation and Cavitation Damage , *Transactions of the ASME* 77, 1045–1054.

Lakshmipathy, S. and V. Togiti (2011) Specific-Dissipation Rate in RANS and Variable-

Resolution Turbulence Models Sunil , *American Institute of Aeronautics and Astronautics* 1–20.

Luo, D., C. Yan, H. Liu and R. Zhao (2014) Journal of Wind Engineering Comparative assessment of PANS and DES for simulation of fl ow past a circular cylinder , *Jnl. of Wind Engineering and Industrial Aerodynamics.* Elsevier 134, 65–77.

Luo, X. W., B. Ji, , Y. Tsujimot. (2016) A review of cavitation in hydraulic machinery, *Journal of Hydrodynamics, Ser. B*, 28, 335–358.

Martynov, S. (2005) Numerical Simulation of the Cavitation Process in Diesel Fuel Injectors , *Analysis*, 1–226.

Moussatov, A., C. Granger and B. Dubus (2005) Ultrasonic cavitation in thin liquid layers, *Ultrasonics Sonochemistry* 12(6), 415–422.

Payri, F., R. Payri, F. J. Salvador and J. Martinez-Lopez (2012) A contribution to the understanding of cavitation effects in Diesel injector nozzles through a combined experimental and computational investigation , *Computers and Fluids* 58, 88–101.

Pendar, M. R. and E. Roohi (2016) Investigation of cavitation around 3D hemispherical head-form body and conical cavitators using different turbulence and cavitation models , *Ocean Engineering* 112, 287–306.

Ranjan, P. and A. Dewan (2015) International Journal of Heat and Mass Transfer Partially Averaged Navier Stokes simulation of turbulent heat transfer from a square cylinder , *Heat And Mass Transfer*. Elsevier Ltd, 89, 251–266.

Salleo, S., A. Nardini, F. Pitt and M. A. Lo Gullo (2000) Xylem cavitation and hydraulic control of stomatal conductance in Laurel (Laurus nobiris L.) , *Plant, Cell and Environment* 23(1), 71–79.

Sharath, S. G. and E. J. Ravi Srinivasan (2003) Pans Turbulence Model For Seamless Transition Between Rans And Les : Fixed-Point Analysis And Preliminary Results , in *February*. Honolulu, Hawaii,USA.

Speziale, C. G. (1996) Computing non-equilibrium turbulent flows with time-dependent RANS and VLES , *Proceedings of 15th International Conference on Numerical Methods in Fluid Dynamics* (1963), 1–7.

Suh, H. K. and C. S. Lee (2008) Effect of cavitation in nozzle orifice on the diesel fuel atomization characteristics , *International Journal of Heat and Fluid Flow* 29(4), 1001–1009.

Travin, A., M. Shur, M. Strelets and P. Spalart (1999) Detached-Eddy Simulations Past a Circular Cylinder , *Flow Turbulence and Combustion* 63, 293–313.

Wang, X. and W. Su (2010) Numerical investigation on relationship between injection pressure fluctuations and unsteady cavitation processes inside high-pressure diesel nozzle holes , *Fuel* 89(9), 2252–2259.

Yan, Y. and R. B. Thorpe (1990) Flow regime transitions due to cavitation in the flow through an orifice , *International Journal of Multiphase Flow* 16(6), 1023–1045.

Yuan, W., J. Sauer and G. H.Schnerr, (2001) Modeling and Computation of Unsteady Cavitation Flows in Injection Nozzles , *Mec. Ind*, 2, 383–394.